AUT Journal of Electrical Engineering
10.22060/EEJ.2026.25681.5987

AI-Enabled Routing in Solar Powered EVS Using Coupled Inductor Sepic Clamp Converter and Optimized MPPT Control

Balaji Viswanathan*[1], Thoudam Basanta Singh[2], Maheswari Ellappan[3], Saravanakumar Sreedevi[4], Tharwin Kumar Ravikumar[5], Ananda Babu Kancherla[6]

[1*]Post-Doctoral Research Scholar, Department of Computer Science and Engineering, Manipur International University, Manipur, India-795140. & Associate Professor, MAI -NEFHI College of Engineering & Technology, Asmara, Eritrea.

[2]Professor, Dean School of Physical Science and Engineering, Manipur International University, Manipur, India- 795140.

[3]Professor, Department of Electrical and Electronics Engineering, Sri Sai Ram Engineering College, Chennai, Tamil Nadu, India-600044.

[4]Associate Professor, Department of Electrical and Electronics Engineering, Sriram Engineering College, Perumalpattu, Chennai, Tamil Nadu, India-602024.

[5]Assistant Professor, Department of Electrical and Electronics Engineering, KPR Institute of Engineering and Technology, Avinashi - Coimbatore Road, Arasur, Tamil Nadu, India-641407.

[6]Assistant Professor, Department of Electrical and Electronics Engineering, SASI Institute of Technology and Engineering, Tadepalligudem, Kadakatla, Andhra Pradesh, India-534101.

* Corresponding Author e-mail: [1]balajieee79@gmail.com

Abstract:

As solar-powered electric vehicles (EVs) become more prevalent, intelligent energy management techniques are necessary to optimise the use of renewable energy and boost system efficiency. For sustainable EV operation, this paper proposes an AI-enabled energy management architecture that combines an optimised maximum power point tracking (MPPT) controller, a Coupled Inductor SEPIC Clamp (CISC) converter and intelligent route prediction. By diminishing input current ripple, lowering switch voltage stress and increasing conversion efficiency, the CISC converter is employed for increasing the Photovoltaic (PV) voltage. A Superb Fairy Optimization-based Radial Basis Function Inference System (SFO-RBFIS) MPPT controller is developed for optimising solar energy extraction under dynamic irradiance and temperature circumstances. It offers quick convergence, excellent tracking accuracy and few steady-state oscillations. Furthermore, an

Artificial Neural Network (ANN) and the SFO Algorithm are employed in a routing strategy that anticipates energy-efficient routing. The developed system attains a converter efficiency of 97.3%, greater MPPT performance and superior energy management when compared to traditional approaches, according to outcomes in the MATLAB tool. The developed framework offers a sustainable and energy-efficient solution for future solar-powered EV systems.

Keywords:

PV system, CISC Converter, SFO-RBFIS-MPPT controller, SFOA-ANN based routing, Battery.

1. Introduction

1-1- Back Ground

The conventional transport system that uses internal combustion engines is the main source of air pollution. In an attempt to diminish air pollution and the transportation industry's reliance on oil, EVs have become more popular in modern centuries [1]. Nevertheless, their widespread use requires robust charging infrastructure, a seamless grid connection, and efficient Energy Management Systems (EMS) to maximise energy utilisation and enhance performance. Effective energy management is vital for EVs to optimise power distribution, increase vehicle performance and reduce energy losses [2]. Over the past few decades, there is a significant shift in the global energy landscape, with a focus on sustainability and a reduction in the environmental impact of fossil fuels [3, 4]. The majority of the world's electricity is produced by fossil fuels in the middle of the 20th century, but worries about resource depletion and greenhouse gas emissions prompted research into RES. Solar technology is become the most extensively employed RES owing to its advantages over other renewable energy sources [5].

PV generation is significantly reduced the cost of solar energy while concurrently increasing energy production and efficiency over time. The Internet of Things is a revolutionary development that has

10.22060/EEJ.2026.25681.5987

enhanced the performance and effectiveness of existing renewable energy systems [6]. The incorporation of IoT into energy generation systems makes the future of renewable energy generation makes vital. Real-time monitoring and management maximise energy reliability and efficiency by incorporating the IOT into energy systems [7]. For effective management practices and policies, dependable real-time IoT system monitoring is essential. As these energy systems get more complex and dependability and efficiency issues arise, the need for a monitoring system becomes clear [8].

2. Literature Survey

A DC/DC converter is vital in a PV-based EV system as the output voltage of solar panels fluctuates and is not appropriately matched to the driving system. A coupled quadratic modified SEPIC converter [9] offers an extensive control variety of switching duty cycle. However, the circuit complexity is increased by using multiple passive components and coupled inductors. Increased voltage stress on the switch and diodes reduces efficiency and necessitates higher-rated components.

High step-up converters with coupled inductors [10] are robust to dissimilarities in output power and offer efficient utilisation of power components. Coupled inductors rise design complexity and expense since they need specific magnetic components. Clamp circuits is need to be installed to avert voltage spikes caused by leaking inductance. The Non-isolated High Step-Up Cuk [11] with Coupled inductors converter significantly diminishes switching losses.

The design of coupled inductors is challenging owing to issues comprising core saturation and magnetic losses. Modular SEPIC-Based Isolated Converters [12] enhance source and load safety and protection by providing electrical isolation. Supplementary magnetic and passive components rise the size and weight of the converter. The efficiency is reduced by circulating currents between modules and transformer losses. An interleaved high step-up [13] converter diminishes input current ripple and boosts source lifetime and efficiency by spreading current over many phases. The control strategy is more complicated since precise phase-shift control and current sharing between phases are required. Additionally, the other recent converters, such as Non-Isolated High Step-Up [14], High Step-Up Boost-Cuk [15], High-Gain Buck-Boost-Cuk [16], Transformer less Active Switched Inductor and Capacitor Cuk [17], and High Step-Up Interleaved Boost-Cuk [18], have maximised efficacy despite having more switch stress, a higher component count, more inrush current and higher costs. To get over the aforementioned challenges, the CISC converter is used in this study.

The inconsistent nature of PV and the sporadic nature of solar irradiation continue to significantly limit reliability and efficiency. Researchers have used MPPT techniques to optimise energy acquisition from solar arrays and wind energy converters to diminish these limitations. Perturb and Observe (P&O) [19], adaptive P&O [20], Model Predictive Control [21] (MPC) and Incremental Conductance (IC) [22] are examples of traditional MPPT algorithms. Nevertheless, these approaches often show degraded performance in quickly fluctuating climatic circumstances, resulting in less than optimal power extraction and diminished system efficiency.

The advancement of AI, particularly since the late 2010s has led to the development of a new generation of intelligent MPPT [23] controllers in response to these boundaries. By using predictive modelling, adaptive learning, and real-time decision-making skills to dynamically adjust to ecological vacillations, these state-of-the-art methods enhance the whole performance of energy harvesting systems [24]. AI- MPPT schemes, like artificial neural networks [25, 26], ANFIS [27] and reinforcement learning frameworks [28], have reliably outperformed traditional techniques, offering more dependable and efficient energy conversion in hybrid systems.

Ant lion algorithm [32], improved voltage scanning method [30], adaptive particle swarm optimisation [29] and arithmetic optimisation algorithm [31]. It precisely tracks the global maximum power point in situations with partial shade and rapidly varying irradiance. Owing to their great computational complexity, many MPPT methods necessitate robust controllers and lengthy processing times.

Incorporated AI and IoT technologies have facilitated the development of sophisticated EV charging environments. Routing is essential for IoT-based EV monitoring systems to offer reliable data transfer between sensors, vehicles and cloud servers. The A* method [33] efficiently predicts the shortest path while reducing unnecessary exploration by combining heuristic guesses and real distance. If the heuristic function is acceptable and consistent, it guarantees an ideal path in IoT-based EV systems, ensuring reliable and predictable routing. The technique takes a lot of memory since it has to keep track of both open and closed lists of nodes, which is an issue for IoT devices with low resources.

Dijkstra's approach [34] is especially reliable for deterministic routing in IoT-based EV monitoring systems since it guarantees the finding of the globally shortest path in a weighted network. It is simple to install and guarantees reliable and consistent performance in a range of network scenarios. Delayed path calculation occurs in large IoT systems since it becomes computationally intensive as the network size rises. Harris-hawk optimisation [35] predicts ideal routing paths even in highly dynamic IoT-based EV systems by adapting its search patterns to node behaviour and network conditions. HHO converge slowly when multiple vehicles or sensors attempt to send data simultaneously, lengthening the routing time.

Binary grey wolf optimisation [36] efficiently reduces energy usage by selecting multi-hop routes that minimise the total transmission cost. Nevertheless, additional fault-tolerant techniques are required since it is challenging to manage sudden node failures or rapid changes in network architecture. The capuchin search technique [37] performs well in dynamic networks when vehicle nodes move or link quality fluctuates and maintains reliable routing under a range of conditions. It is scalable to large networks with many nodes and vehicles since it provides consistent performance without significantly lowering routing efficiency. Convergence speed is slowdown in highly congested networks, causing longer delays in route selection and data transfer. Although having the highest computational overhead, the MFO-AOA [38] diminishes energy consumption. Although GA-PSO [39] is more sophisticated, it is appropriate for robust circumstances and diminishes maximum hop counts. To increase the effectiveness, the research develops an SFOA-ANN for routing.

2-1- Research Gap

10.22060/EEJ.2026.25681.5987

While present converters and MPPT approaches enhance PV energy extraction, they frequently have significant computational complexity, slow convergence, higher switching stress and poor performance under circumstances of rapidly varying irradiance. Also, existing IoT-enabled EV routing algorithms prioritise shortest-path optimisation above coordinated control of PV generation, battery SOC and real-time vehicle energy demand. Thus, to rise energy efficiency and system dependability in solar-powered electric vehicles, a single framework that concurrently optimises power conversion, energy management, and routing is required.

. The main objectives are,

- The development of the CISC converter ensures the enhanced voltage under fluctuating PV and load conditions.
- The SFO-RBFIS-MPPT controller, which ensures reduced power oscillations and enhanced transient response.
- By stowing extra PV energy and supplying electricity during times of high demand or low sunlight, the battery system is employed.
- The SFOA-ANN routing algorithm intelligently manages the flow of energy between the battery, PV array and motor.

The residue of this work is arranged as: A review of relevant literature is covered in Section 2. The developed system's architecture, routing protocols and optimization methods are described in depth in Section 3. Section 4 presents the experimental outcomes and discussions. This paper is finally concluded in Section 5.

3. Proposed Methodology

The AI-enabled energy management and routing architecture for a solar-powered EV system is depicted in Figure 1. The main renewable energy source is the PV array, which generates a nonlinear DC output that is influenced by temperature and irradiance. A CISC converter is employed to effectively rise PV power while

10.22060/EEJ.2026.25681.5987

diminishing voltage spikes, switch voltage stress and input current ripple via an active clamp circuit. Fast transient response and precise torque regulation are ensured by the steady DC-link that offers a three-phase VSI to drive the BLDC traction motor using PWM-based closed-loop speed control with PI controllers. To maintain power balance and increase battery utilisation, a bidirectional converter simultaneously attaches the battery system with the DC bus. This permits controlled charging during excess PV generation and discharging in peak load or low irradiance circumstances. In order to perform the MPPT, motor control and energy management algorithms with deterministic timing and minimal latency, an FPGA-based controller obtains real-time measurements. Furthermore, by learning the nonlinear correlations amid PV power availability, battery SOC, vehicle operating conditions and load demand, the SFO-ANN predicts energy-efficient travel routes and reducing energy consumption.

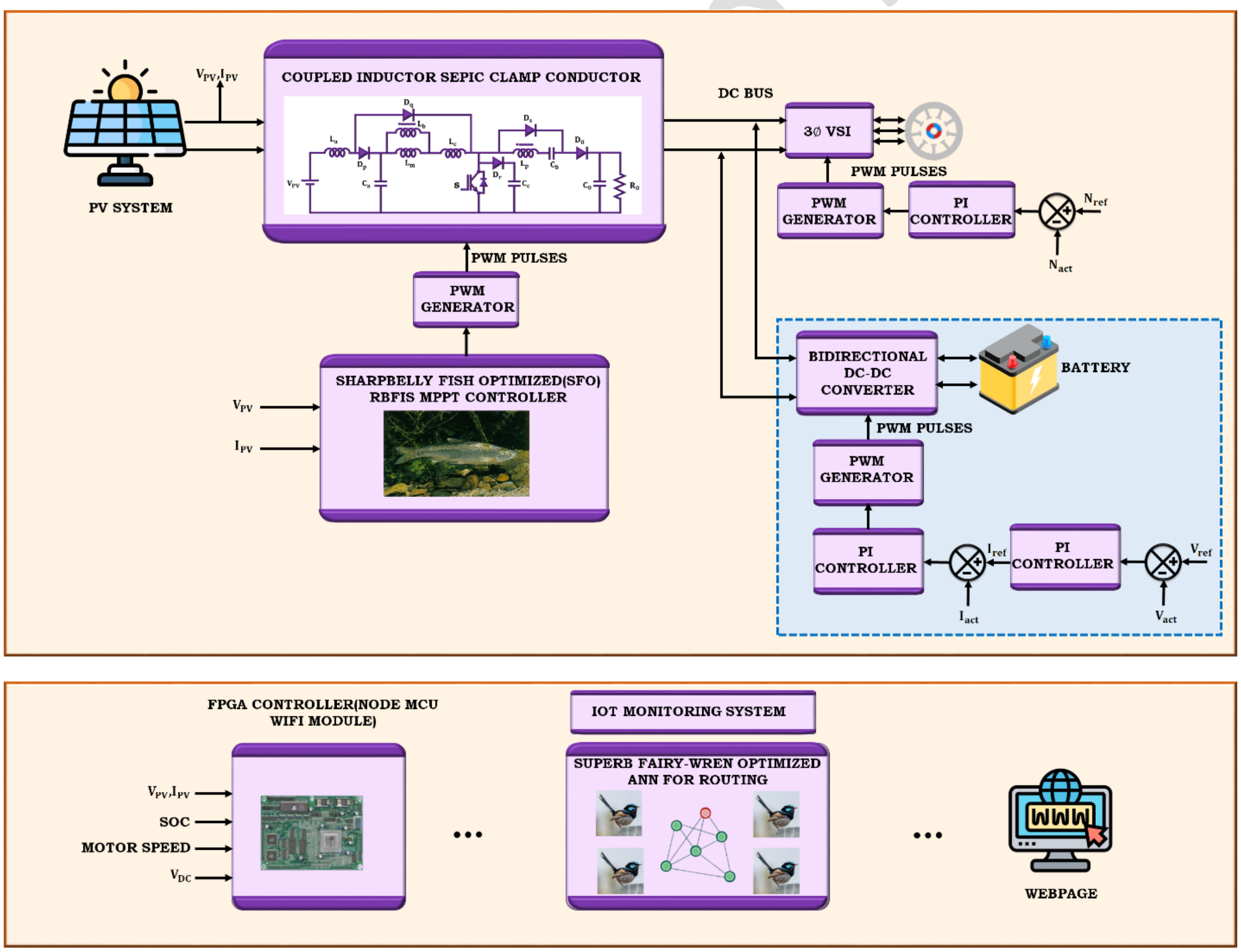

AUT Journal of Electrical Engineering
10.22060/EEJ.2026.25681.5987

Fig. 1. Block diagram of AI-enabled routing system

Through a web interface, an IoT-enabled monitoring platform increases system observability and operational reliability by offering real-time visualisation, remote diagnostics and performance analytics. A highly effective and dependable energy management framework for next-generation solar-powered electric vehicles is generated by the coordinated operation of the CISC converter, intelligent MPPT controller, bidirectional battery management, FPGA-based real-time control, routing and IoT monitoring.

3-1- PV System

As depicted in Fig. 2, the single-diode representation describes the mathematical description of the PV cell. Cell current in the previously mentioned paradigm is defined by the PV Equation (1).

$$I_{PV} = I_{PH} - I_0 \times (\frac{q(V_{PV} + R_S * I_{PV})}{akT} - \frac{(q(V_{PV} + R_S * I_{PV})}{R_{Sh}} \qquad (1)$$

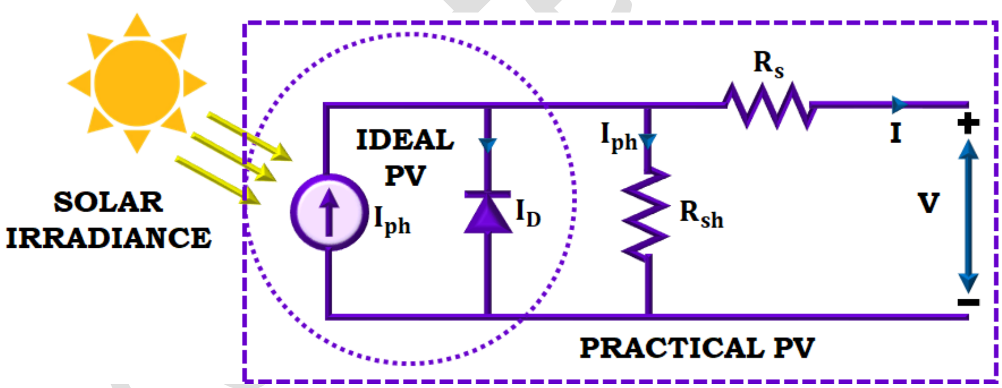

Fig. 2. Circuit of PV system

Where, T is the temperature, V_{PV} and I_{PV} are the PV's voltage and current, I_{PH} is the current source, and k is the Boltzmann constant. Numerous material characteristics affect I_{ph} of a solar cell. Nonetheless, it is sufficiently predicted to be linearly dependent on temperature and irradiance, as

$$I_{PH} = \frac{G}{G_{ref}} \left[I_{sc,ref+} \mu_{sc} \left(T - T_{ref} \right) \right] \qquad (2)$$

Where $I_{sc,ref}$ is the solar cell's short-circuit current. Diode saturation current is,

10.22060/EEJ.2026.25681.5987

$$I_0 = I_{0,ref}\left(\frac{T_{ref}}{T}\right)^3 e\left[\frac{q}{nk}\left(\frac{1}{T_{ref}} - \frac{1}{T}\right)\right] \tag{3}$$

The nominally saturated current is,

$$I_{0,ref} = \frac{I_{sc,ref}}{e\left(\frac{V_{oc,ref}}{nV_t}\right) - 1} \tag{4}$$

Where the open circuit voltage (reference) is denoted by $V_{oc,ref}$.The CISC converter increases the PV voltage, which is caused by environmental variations.

3-2- CISC Converter

The coupled inductor SEPIC clamp converter is employed for raising PV voltage high-performance power conversion applications since it provides reduced component stress, increased efficiency and high voltage gain. The clamp network, which consists of C_o, capacitors C_b, C_a, C_cdiodes $D_q, D_p, D_r, D_s and\ D_o$ shields the active switch from voltage spikes and increases dependability by absorbing leakage energy from the associated inductors. As presented in Fig. 3, the coordinated action of inductors, diodes and capacitors during switching cycles ensures smooth current transitions, decreased switching losses and less electromagnetic interference.

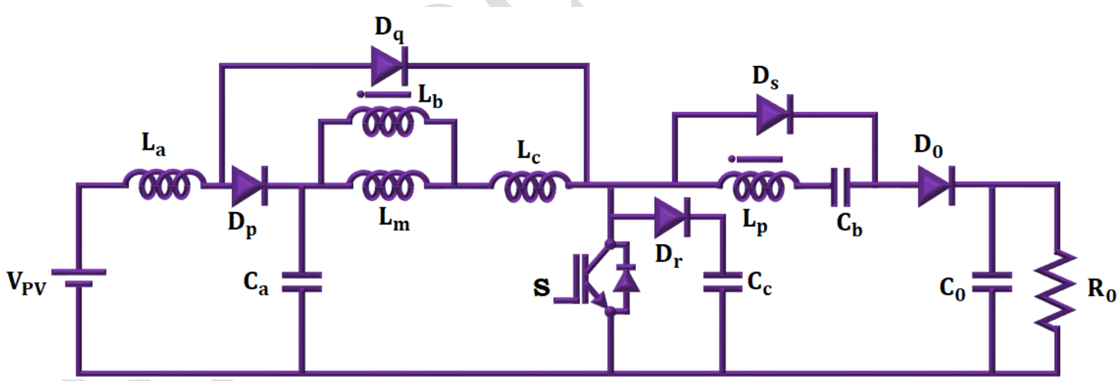

Fig. 3. Circuit of CISC converter

Stage 1

As displayed in Fig. 5(a), in Mode 1, $D_r$and C_c are is in the OFF state, meaning that no current flows through them and the switch S is turned ON. When L_a and $L_b$start to store energy from V_{PV} , the current flowing via $L_b\ and\ L_a$ increases linearly.

10.22060/EEJ.2026.25681.5987

$$V_{PV} - V_{L_a} = 0 \tag{5}$$

$$V_{PV} - V_{C_b} - V_{L_b} = 0 \tag{6}$$

$$V_{PV} - L_a \frac{di_{L_a}}{dt} - V_S = 0 \tag{7}$$

$$V_{PV} - V_{C_b} - L_b \frac{di_{L_b}}{dt} - V_S = 0 \tag{8}$$

$$V_{C_0} - i_o R = 0 \tag{9}$$

$$i_o = \frac{V_{C_0}}{R} \tag{10}$$

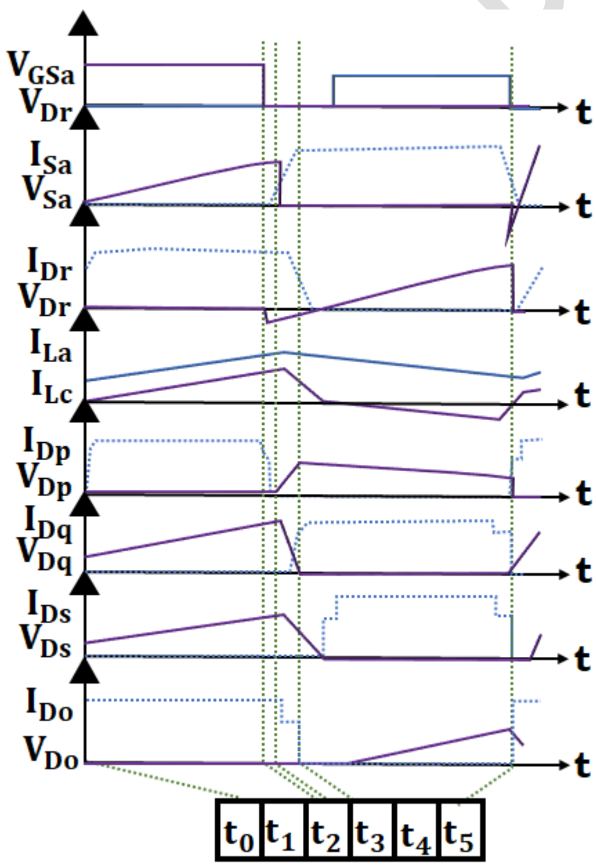

Fig. 4. Switching waveform of CISC converter

Stage 2

10.22060/EEJ.2026.25681.5987

The energy held in the L_b and $L_a$is released in Mode 2 when the switch S, D_r and C_c are switched off. The clamp capacitor remains unattached while this energy is partially transported to C_o and the load. Energy flow to the output is maintained by the input inductorL_a continuing to supply current via the loop established by the output diode andL_b as indicated in Fig. 5(b). By releasing its stored energy via the output channel, the coupled inductorL_b contributes to boosting the voltage at V_{C_0}.

$$V_{L_a} + V_{C_0} = V_{in} \tag{11}$$

$$V_{L_a} = V_{in} - V_{C_0} \tag{12}$$

$$V_{L_b} + V_{C_0} = 0 \tag{13}$$

$$V_{L_b} = -V_{C_0} \tag{14}$$

$$V_{C_0} - i_o R - V_{L_a} = 0 \tag{15}$$

$$i_o = \frac{V_{C_0} - V_{L_a}}{R} \tag{16}$$

$$\frac{di_{L_a}}{dt} = \frac{V_{in} - V_{C_0}}{L_a} \tag{17}$$

$$\frac{di_{L_b}}{dt} = \frac{-V_{C_0}}{L_b} \tag{18}$$

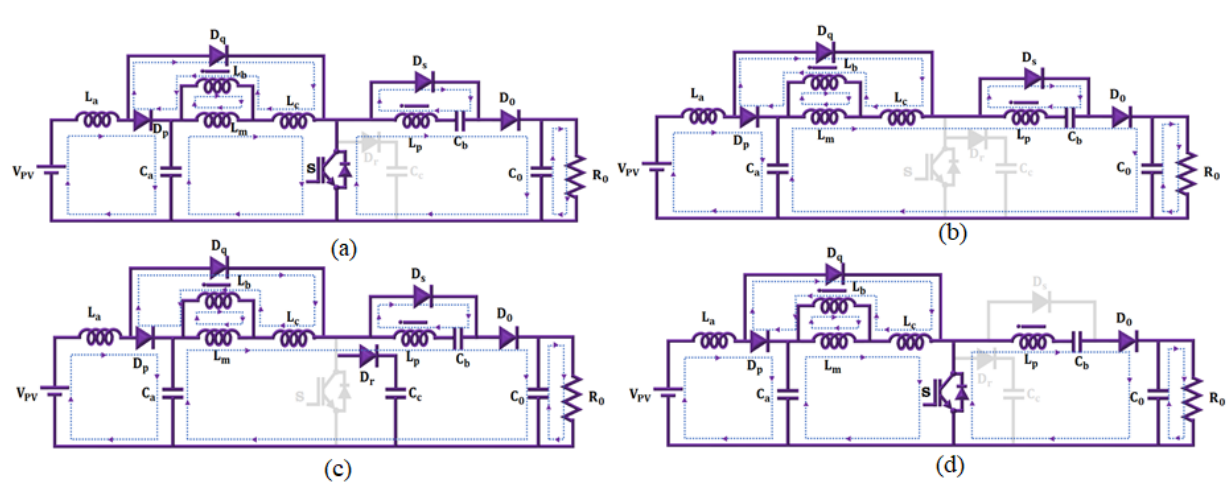

AUT Journal of Electrical Engineering
10.22060/EEJ.2026.25681.5987

Fig. 5. (a) Stage 1(b) Stage 2 (c) Stage 3 (d) Stage 4 of CISC converter

Stage 3

As depicted in Fig. 5(c), in Mode 3, S is turned off andD_r andC_c begins to conduct in response to the inductor currents, allowing the leakage energy stowed in the linked inductor to be partially transferred to the clamp capacitor. The energy stowed in L_b and L_a continues to flow to C_o and the load while the switch is idle, raising the output voltage. D_r is conduct if the voltage across C_c permits, charging the clamp capacitor and lessening the voltage spike across S. As energy is provided to the clamp and C_o , the inductors' currents decrease linearly while the output capacitor keeps the load voltage constant.

$$V_{L_b} = V_{in} - V_{C_b} - V_{C_0} \tag{19}$$

$$V_{C_0} - i_o R = 0 \tag{20}$$

$$i_o = \frac{V_{C_0}}{R} \tag{21}$$

$$\frac{diL_a}{dt} = \frac{V_{in} - V_{C_0} - V_{D_r}}{L_a} \tag{22}$$

$$\frac{diL_b}{dt} = \frac{V_{in} - V_{C_b} - V_{C_0}}{L_b} \tag{23}$$

Stage 4

The converter is supplying the load via C_o because $D_r$and D_s are OFF and the energy stored in$L_a$and L_b has mostly been transferred to the output. As depicted in Figure 5(d), there is minimal voltage stress across S and no energy flows to the clamp capacitor $C_c$since the inductors are still discharging but the routes through$D_r$and D_s are blocked. At this point, C_o provides the majority of the load current.

$$V_{L_a} = -V_{C_0} \tag{24}$$

$$V_{L_b} = -V_{C_0} \tag{25}$$

$$V_{C_0} = -_{i_0} R = 0 \tag{26}$$

10.22060/EEJ.2026.25681.5987

$$i_0 = \frac{V_{C_0}}{R} \tag{27}$$

$$\frac{diL_a}{dt} = -\frac{V_{C_0}}{L_a} \tag{28}$$

$$\frac{diL_b}{dt} = -\frac{V_{C_0}}{L_b} \tag{29}$$

$$V_{L_a}^{ON} = V_{in}, V_{L_b}^{ON} = V_{in} - V_{Cb} \tag{30}$$

$$V_{L_a}^{OFF} = V_{in} - V_{C0}, V_{L_b}^{OFF} = V_{in} - V_{Cb} - V_{C0} \tag{31}$$

By applying volt-second balance law,

$$V_{L_a}^{ON} D + V_a^{OFF} \quad) = (1-D) = 0 \tag{32}$$

$$V_{in} D + \left(V_{inV_{co}}\right)(1-D) = 0 \tag{33}$$

$$V_{in} D + V_{in}(1-D)(1-D) = 0 \tag{34}$$

$$V_{C_0}(1-D) = V_{in} = V_{C_0} = \frac{V_{in}}{1-D} \tag{35}$$

$$V_{L_b}^{OFF} = V_{in} - V_{C_b} - V_{C_0} = V_{C_0} = \frac{V_{in}(1+n)}{1-D} \tag{36}$$

The obtained voltage gain is,

$$G = \frac{VC_0}{V_{in}} = \frac{1+n}{1-D} \tag{37}$$

In this research, the SFO-RBFIS-MPPT controller is mainly utilized to maximize the power extraction from PV system.

3-3- SFO-RBFIS-MPPT Controller

The goal of the RBFIS- MPPT controller is to produce an optimum control signal (duty cycle or reference voltage/current) that forces the PV system to operate at its MPP in a range of environmental circumstances. The three main components of the RBFIS are developed by an input layer, fuzzification layer and a

10.22060/EEJ.2026.25681.5987

defuzzification layer. The MPPT controller employs the RBFNN to efficiently track the MPP of the PV system. The k^{th} output of the RBFNN is,

$$O_k = B_0 + \sum_{j=1}^{n} wjk * H_j \tag{38}$$

Where, the center is c and the hidden unit's radial basis output is H_j.

$$H_j = \left(1 - C_j\right) \tag{39}$$

$$f\left(x\right) = e\frac{-\left(l_i - c_i\right)\Lambda 2}{r^2} \tag{40}$$

$$c_i = I_i - C_j \tag{41}$$

Where $f(x)$ is the Gaussian function. Fuzzy logic is incorporated with RBFNN for MPPT using a fuzzy inference method, which permits the PV system to function at extreme power in variable load, temperature and irradiance. The fuzzy MPPT comprises of three stages, fuzzification, inference engine and defuzzification. Fuzzification is the process of transforming sharp input values, like PV power and voltage into fuzzy language variables. The error $(err)$and error change $(derr)$ as,

$$err\left(k\right) = \frac{P_{pv}\left(k\right) - P_{pv}\left(k-1\right)}{V_{pv}\left(k\right) - V_{pv}\left(k-1\right)} \tag{42}$$

$$err\left(k\right) = \frac{P_{pv}\left(k\right) - P_{pv}\left(k-1\right)}{V_{pv}\left(k\right) - V_{pv}\left(k-1\right)} \tag{43}$$

The surfaces produced by each activated rule are combined to make the overall fuzzy outcome. Defuzzification transforms the fuzzy output into a clear value so that the PV system is managed. The function of custom defuzzification is,

$$Z_{COA} = \frac{\int \mu_A\left(z\right) zdz}{\int \mu_A\left(z\right) zdz} \tag{44}$$

Where, the control output is Z_{COA}.

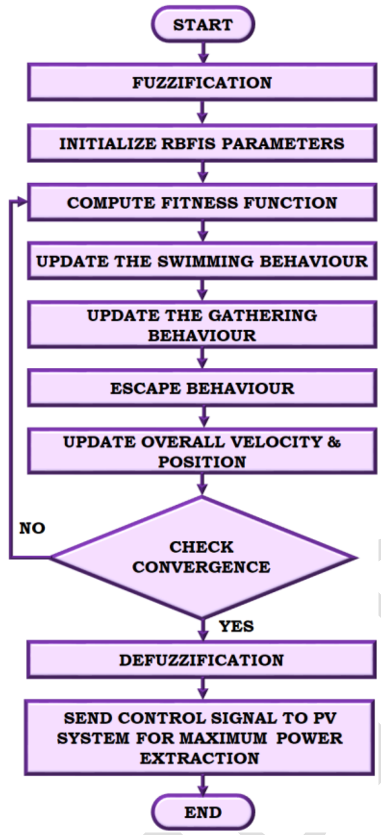

Fig. 6. Flowchart of SFO-RBFIS-MPPT controller

Each sharp belly fish's location is indicated as a point in a D-dimensional space, D is the total amount of RBFIS parameters that is adjusted. These parameters comprise the radial basis membership functions' centers, widths and output weights. A single complete candidate parameter set of the RBFIS controller is denoted by each sharp belly fish. Fig. 6 represents the SFO-RBFIS-MPPT controller's flowchart. Within the predetermined feasible constraints of RBFIS parameters, the initial population matrix is produced at random by,

$$X^{0} = rand\left(N, D\right)\left(ub - lb\right) + lb \tag{45}$$

One entire candidate solution for the RBFIS-based MPPT controller is indicated by each sharpbelly fish. In particular, all configurable RBFIS parameters, like the radial basis function centers, output-layer weights, Gaussian widths and bias term, are encoded in the position vector Xi. An objective function that seeks to

10.22060/EEJ.2026.25681.5987

maximise the extracted PV power while diminishing steady-state oscillations during MPPT operation is utilized to evaluate each candidate RBFIS controller's quality. The fitness of each individual is estimated by an objective function with outcomes are stored in F^t.

$$F^t = f\left(X_1^t\right), f\left(X_2^t\right), \ldots, f\left(X_N^t\right)^T] \tag{46}$$

Where $f(\cdot)$ signifies the MPPT performance indicator. Iterative SFO position updates simultaneously enhance the RBFIS's centers, widths and weights, directing the population toward an ideal fuzzy inference structure that produces fast, precise and dependable MPPT under varying temperature and irradiance circumstances. During the swimming and gathering phase, the SFO algorithm adaptively fine-tunes the RBFIS-MPPT controller settings by balancing exploration and exploitation around the currently ideal controller configuration. To alter the RBF centers, widths and output weights in the direction of the global optimum solution, each sharpbelly fish that indicates a potential RBFIS parameter vector X_i^t is given a fitness-dependent swimming behaviour. The vector of swimming velocity is,

$$V_i^{swim} = S_i^t .rand().\left(X_{best}^t - X_i^t\right). \tag{47}$$

$$S_i^t = 1 - \frac{f(X_i^t)}{max_i\, f(X_i^t) + \in} \tag{48}$$

Here, S_i^t is the adaptive swim speed. The MPPT performance index of the RBFIS controller that i^{th} fish encodes is denoted by $f(X_i^t)$. Deeper exploration of the controller parameter space is encouraged by this technique, which ensures that high-quality solutions undergo fewer refinements while poorly performing RBFIS configurations, characterized by improved tracking error or power oscillations, display bigger parameter variations. Concurrently, a gathering way is implemented to force collective convergence toward the most prevalent RBFIS parameter set as, irrespective of individual fitness,

$$V_i^{gather} = \alpha.rand.\left(X_{best}^t - X_i^t\right). \tag{49}$$

Each fish's position and the RBFIS parameters are updated by a combination of swimming and gathering behaviours. In the environmental variations, this permits rapid convergence towards an ideal fuzzy inference

10.22060/EEJ.2026.25681.5987

structure that maximises extracted PV power while maintaining rapid and stable MPPT dynamics. The SFO algorithm provides a controlled stochastic disturbance during the escape behaviour phase to avert early convergence. This method simulates the natural response of sharp belly fish to unexpected environmental shocks by permitting individual fish, each stowing a complete RBFIS parameter vector consisting of radial basis centers, widths and consequent weights to abruptly explore new parts of the search space. The disturbance velocity is,

$$V_i^{disturb} = \begin{cases} \delta . N(0,1), if \;\; ran < Pf \\ 0 \; , otherwise \end{cases} \tag{50}$$

Where $N(0,1)$ is a D-dimensional standard Gaussian random vector, δ manages the amount of perturbation given instantaneously to all RBFIS parameters and Pf indicates the disturbance probability. By providing abrupt variations in the membership function centers, spreads and output weights of the RBFIS-MPPT controller, this escape behaviour permits the algorithm to escape from local optima caused by nonlinear PV characteristics or quickly varying irradiance circumstances. A larger Pf encourages global exploration in early optimisation phases, increasing convergence reliability and resilience of the enhanced MPPT controller, while smaller values preserve parameter stability and fine tuning in succeeding iterations.

Stagnation is detected when a single sharp belly fish, which serves as a possible RBFIS parameter vector. After this criterion is met, a dispersal velocity is applied, compelling the person to explore a new region of the controller parameter space to evade entrapment in local optima brought by nonlinear PV dynamics. The dispersal mechanism is,

$$V_i^{disperse} = \begin{cases} \gamma . \, (2.rand() - 1(ub - lb), if \;\; c_{no\_improve} \geq T_s \\ 0 \; , otherwise \end{cases} \tag{51}$$

By selectively activating this mechanism only during stagnation, the SFO strategy preserves convergence efficiency while ensuring sufficient diversity to develop a globally optimal RBFIS-MPPT controller with greater tracking accuracy and dynamic performance. During the position update phase, the SFO algorithm

10.22060/EEJ.2026.25681.5987

incorporates numerous physiologically inspired behaviours to perform a uniform update of the RBFIS-MPPT controller settings. The total velocity at iteration t is calculated by superimposing the contributions of swimming, gathering, escape and dispersal behaviours.

$$V_i^t = V_i^{swim} + V_i^{gather} + V_i^{disturb} + V_i^{disperse} \tag{52}$$

The related controller parameter set is updated as,

$$X_i^{t+1} = X_i^t + V_i^t \tag{53}$$

$$X_i^{t+1} = min\left(\max\left(X_i^{t+1}, lb\right), ub\right) \tag{54}$$

Following each position update, all optimised RBFIS parameters are limited to ensure practical and steady controller functioning. Only the normalised input domain is employed for the radial basis centers.

$$c_j \in \left[c_{min}, c_{max}\right] \tag{55}$$

Where c_{min} and c_{max} are the normalised MPPT input variables' minimum and maximum values. The Gaussian widths satisfy,

$$\sigma_j \in \left[\sigma_{min}, \sigma_{max}\right], \sigma_j > 0 \tag{56}$$

According to Eq. (54), an updated parameter is projected back into the feasible region whenever it surpasses its permitted interval.

$$\omega_j, B_0 \in \left[\omega_{min}, \omega_{max}\right] \tag{57}$$

To verify feasibility and stable controller characteristics, each updated RBFIS parameter is constrained within predetermined bounds using a projection operator.

$$X_{best}^{t+1} = \begin{cases} X_i^{t+1}, \; if \;\; fX_i^{t+1} < f(X_{best}^t) \\ X_{best}^t, \qquad\qquad\qquad otherwise \end{cases} \tag{58}$$

This iterative velocity-based update method guarantees a fair trade-off amid local exploitation and global exploration. By unceasingly holding onto the best-performing RBFIS-MPPT controller and guiding succeeding fish movements, the SFO algorithm converges toward an ideal fuzzy inference structure that maximises PV power extraction while preserving rapid dynamic response and robustness under numerous operating circumstances.

3-4- BLDC Motor

The BLDC motors are electronically regulated and not necessitate brushes or commutators, they offer superior overall performance and efficiency. The performance of the BLDC motor is,

$$V_t(s)=E_s(s)+(R_s+sL_s)I_s(s) \tag{59}$$

$$E_s(s)=KE\omega_r(s) \tag{60}$$

$$T_e(s)=k_T I_s(s) \tag{61}$$

$$T_e(s)=T_L(s)+(B+sJ)\omega_r(s) \tag{62}$$

The transfer function of BLDC motor is,

$$\omega_r(s)=\frac{k_T}{(R_s+sL_s)(sJ+B)+k_T k_E}V_t(s)+\frac{R_s+sL_s}{(R_s+sL_s)(sJ+B)+k_T k_E}T_L(s) \tag{63}$$

Here, $V_t(s)$ is the stator terminal voltage, k_E is the back EMF constant, $I_s(s)$ is the stator phase current, $T_e(s)$ is the electromagnetic torque, $T_L(s)$ is the load torque, $\omega_r(s)$is the rotor angular speed, $E_s(s)$ is the back EMF, L_s and $R_s$are the stator phase inductance and resistances and B is the friction coefficient.

3-5- Battery

To preserve a steady power supply, the battery is employed to store extra energy produced and release it when necessary, like at night or on overcast days. In this case, open circuit voltage is indicated by E_b and internal resistance by R_{bat} . The voltage of the battery is,

$$V_{bat}=E_b-I_{bat}R_{bat} \tag{64}$$

If $I_{bat}(k)<0$,

10.22060/EEJ.2026.25681.5987

$$SOC(k) = SOC(k-1) - \frac{\eta_{chrg} I_{bat}(k) \Delta t}{C_{bat}} \quad (65)$$

If $I_{bat}(k) > 0$,

$$SOC(k) = SOC(k-1) - \frac{I_{bat}(k) \Delta t}{\eta_{dischrg} C_{bat}} \quad (66)$$

Where, the battery's charging and discharging efficiencies are η_{chrg} and $\eta_{dischrg}$, battery's nominal capacity is C_{bat},

$$\eta_{chrg} = \eta_{dischrg} = \sqrt{\eta_{bat}, rt} \quad (67)$$

Where, (η_{bat}, rt) indicates the round-trip efficiency.

3-6- SFOA-ANN Based Routing

The SFOA–ANN routing is developed to offer low-latency, and energy-efficient communication for the IoT-enabled solar-powered EV monitoring system. Using a wireless mesh architecture, 100 IoT sensor nodes are dispersed at random within a 500 m x 500 m geographic area to form the monitoring network. Battery state, PV generation, motor operating conditions, temperature, and environmental data are periodically reported by each node, which has sensing, processing and communication abilities. Owing to its low power consumption and adaptability for IoT applications, the IEEE 802.15.4 standard is adopted at the Physical (PHY) and Medium Access Control (MAC) levels, while the network layer manages adaptive multi-hop routing. Each node shares routing data with its adjacent nodes, like residual energy, packet queue occupancy, hop distance, communication delay, received signal strength (RSSI), link quality indicator (LQI) and traffic load. Under dynamic network settings, intelligent next-hop selection is made by the routing metrics that develop the ANN's input feature vector. While the hidden layer uses sigmoid activation functions to extract nonlinear correlations among the routing metrics, the input layer gets the routing parameters. The output layer predicts the best routing path by computing each neighbouring node's forwarding appropriateness score. The input characteristics' weighted sum is computed as,

10.22060/EEJ.2026.25681.5987

$$t_i = \sum_{j=1}^{n} W_{ij} X_j \tag{68}$$

If X is the input data from node j, W is the interconnection weight amid nodes $i\ and\ j$ and n is the number of inputs. The node output value O_i is analysed by the transfer function in the weighted value of the ANN model. Both the hidden and output layers of the ANN model employ the sigmoidal function, which is the most extensively utilised transfer function. The linear transfer function is employed by the input layer as,

$$O_i = f(t_i \tag{69}$$

Finally, the chain rule is used to compute the error subordinate based on the weight value. The parameters of SFOA is depicted in Table 1.

Table 1 Parameters of SFOA

Parameter	**Value**
Levy flight	1.5
Maximum iterations	100
Adaptive coefficient	0.5
Population size	30
Scaling coefficient	1
Random variables	(0,1)

The activated neuron output is,

$$t_i = \phi(net) \tag{70}$$

To efficiently capture the nonlinear aspects of routing decisions, this model employs nonlinear activation functions in the hidden and output layers while applying a linear activation function at the input layer. The neuron net input is,

$$net = \sum_{j=1}^{n} W_{ij} X_j \tag{71}$$

10.22060/EEJ.2026.25681.5987

Back propagation is employed in the ANN training process to diminish the routing error. The chain rule is employed to compute the gradient of the error with regard to each connection weight as,

$$\frac{\delta E}{\delta W_{ij}} = \frac{dE}{dt_i} \times \frac{dt_i}{d_{net}} \times \frac{d_{net}}{\delta W_{ij}} \tag{72}$$

Where, the error change proportional to the weighted sum change is $\frac{\delta E}{\delta W_{ij}}$, error change proportional to the output change is $\frac{dt_i}{d_{net}}$ and weighted sum change is $\frac{d_{net}}{\delta W_{ij}}$. Even though ANN learning is a superior for nonlinear routing decisions, delayed convergence and entrapment in local minima frequently restrict its efficacy. The SFOA is employed to optimise the ANN parameters, like learning rate, synaptic weights, bias values and hidden neurone parameters to get over these disadvantages. The fitness function assesses routing quality by concurrently maximising packet delivery ratio and network lifetime and jointly minimising packet loss, communication delay, energy consumption and hop count. Each fairy-wren individual corresponds to a comprehensive ANN parameter vector. First, the SFOA develops a population of potential ANN solutions at random inside the specified search parameters based on,

$$X_i^{ini} = lb + rand(1, D) \times (ub - lb) \tag{73}$$

Every initialized solution specifies a whole ANN configuration that generates routing decisions by processing routing inputs like node energy, hop distance, delay and link stability. Fig. 7 illustrates the flowchart of SFOA-ANN based routing.

10.22060/EEJ.2026.25681.5987

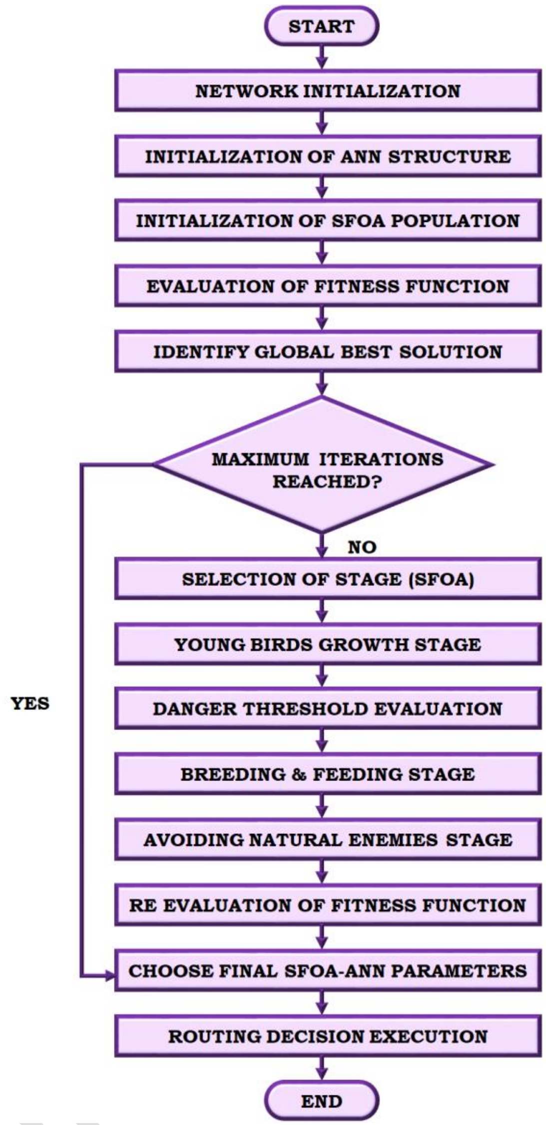

Fig. 7. Flowchart of SFOA-ANN based routing

SFOA conducts global exploration in the growing stage of young birds by generating a variety of ANN parameter combinations that fully explore the search space and avert early convergence. The candidate solution is updated as,

$$X_i^{new} = X_i^{old} + rand\left(1, D\right) \times \left(ub - lb\right) + lb \tag{74}$$

10.22060/EEJ.2026.25681.5987

The ANN predict numerous routing options throughout this exploration period before converging toward viable solutions. The optimisation then moves on to the Breeding and Feeding Stage, where the search concentrates on exploiting the globally optimal ANN solution. The ANN's parameters are enhanced using,

$$X_i^{new} = a \times X_{best} + \left(X_{best} - X_i^{old}\right) \times \sin\left(ub - lb\right) \times \left(2 + \frac{2FEs}{MaxFEs}\right) \tag{75}$$

The current fitness evaluation is FEs, the highest allowable current fitness evaluation is $MaxFEs$, the adaptive factor is $\left(2 + \frac{2FEs}{MaxFEs}\right)$ and the current and updated ANN parameter sets are X_i^{new} and X_i^{old}. Through this technique, PSFWO adjusts ANN settings to diminish routing cost metrics like as hop count, latency and energy usage. Table 2 represents the pseudocode of SFOA-ANN based routing.

Table 2 Pseudocode of SFOA-ANN based routing

$Input$:
$G, N, Np, MaxIter, ANN, lb, ub, RoutingMetrics$
$Output$:
$Xbest, BestRoute$
$Begin$
1. $Deploy\ N\ sensor\ nodes\ and\ initialize\ the\ ANN.$
2. $Generate\ Np\ fairy-wrens\ (Xi), where\ each\ Xi\ represents$
$ANN\ weights, biases, and\ learning\ parameters.$
3. $Evaluate\ the\ fitness\ Fi\ of\ each\ Xi\ and\ determine\ Xbest.$
4. $For\ Iter\ =\ 1\ to\ MaxIter\ do$
$For\ each\ Xi\ do$
$Select\ an\ SFOA\ search\ stage$:
• $Young\ Birds\ Growth\ (Exploration)$
• $Breeding\ and\ Feeding\ (Exploitation)$

10.22060/EEJ.2026.25681.5987

- $Avoiding\ Natural\ Enemies\ (Diversification)$

$Update\ Xi\ according\ to\ the\ selected\ stage.$

$Restrict\ Xi\ within\ [lb, ub].$

$Evaluate\ Fi.$

$If\ Fi\ is\ better\ than\ Fbest\ then$

$Update\ Xbest.$

$End\ If$

$End\ For$

$End\ For$

5. $Load\ the\ optimized\ ANN\ parameters\ (Xbest).$

6. $For\ each\ data\ packet\ do$

$Collect\ RoutingMetrics\ from\ neighboring\ nodes.$

$Compute\ RoutingScore\ using\ ANN.$

$Select\ the\ neighbor\ with\ the\ highest\ RoutingScore.$

$Forward\ the\ packet\ to\ the\ selected\ next-hop.$

$End\ For$

7. $Return\ BestRoute.$

End

By lowering energy consumption, routing overhead, transmission latency and hop count, this adaptive refinement rises routing accuracy. The Avoiding Natural Enemies Stage, which comprises adaptive perturbations inspired by the predator-avoidance behaviour of superb fairy-wrens, is incorporated into SFOA to further increase optimisation robustness. This method rises convergence variability while averting stagnation in local optima. The vector of ANN parameters is updated in accordance with,

10.22060/EEJ.2026.25681.5987

$$X_i^{new} = X_{best} + X_i^{old} \times l \times b \times \sin(\frac{\pi}{2} \times \left(1 - \frac{FEs}{MaxFEs}\right) \tag{76}$$

At each iteration, the SFOA probabilistically chooses one of three behavioural stages to update the population of ANN parameter vectors for shortest-path routing in the EV monitoring system. As a consequence, the SFOA unified execution method for ANN parameter vector update is,

$$s = r2 \times 20 + r3 \times 20 \tag{77}$$

$$X_i^{new} = \begin{cases} X_i^{old} + rand(1, D), \times (ub - lb) + lb, r_1 > 0.5 \\ a \times X_{best} + \left(X_{best} - X_i^{old}\right) \times sin((ub - lb) \times \left(2 + \frac{2FEs}{MaxxFEs}\right) r_1 \le 0.5 and\, s \le 20 \\ X_{best} + X_i^{old} \times l \times b \times sin(\frac{\pi}{2} \times \left(1 - \frac{FEs}{MaxFEs}\right), r_1 \le 0.5 and\, s > 20 \end{cases} \tag{78}$$

The ANN continually evaluates all nearby nodes after optimisation by analysing their residual energy, hop distance, communication delay, connection quality, traffic load and queue occupancy. In order to provide adaptive route recovery without undue control overhead, route discovery and maintenance are repeated anytime notable topology modifications or link failures are recognised. For the IoT-enabled solar-powered EV monitoring network, the SFOA–ANN routing algorithm thus strikes a balance between local exploitation and global exploration during ANN optimisation, permitting intelligent shortest-path routing with minimal energy consumption, decreased latency, enhanced packet delivery ratio, extended network lifetime and extremely dependable communication.

4. Result and Discussion

The outcomes of AI-enabled routing in solar-powered EVs are examined in this section by the MATLAB tool and its effectiveness is validated by the analysis comprised in this section. The parameters of this study are revealed in Table 3.

Table 3. Specification of parameters

Parameters	Specification

10.22060/EEJ.2026.25681.5987

PV system	
Total Power	10000 W
Parallel strings	15
Series connected modules	10
Voltage (Open circuit)	37.5V
Module	Aleo solar s18y250
Temperature coefficient of V_{oc}	-0.314
Maximum power	249.672
Cell per module	60
Maximum Peak Current	8.35 A
Temperature coefficient of I_{sc}	0.043995
Current (Short circuit)	8.76 A
No of cells in shunt connection, N_P	3
CISC converter	
C_a, C_b, C_c	22 μF
L_a, L_c	4.7mH
C_O	2200 μF
Switching frequency	10kHz
PMBLDC Motor	
R_s	2.3
L_s	7.68e-3
Back EMF flat area	120
Torque constant	0.74
When theta=0 , rotor flux position	90 degrees behind phase A axis
Battery	
Nominal voltage (V)	420
Initial state-of-charge (%)	80
Battery response time (s)	30
Type	Lead-Acid
Rated capacity (Ah)	10

10.22060/EEJ.2026.25681.5987

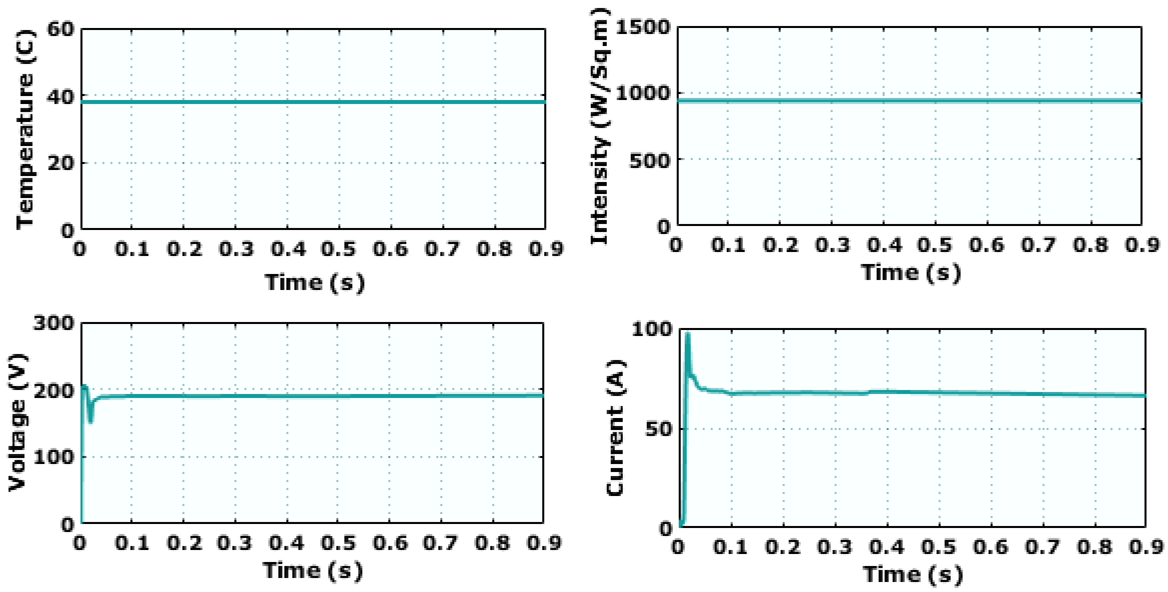

Fig. 8. Responses of PV system in constant scenario

The PV system's response under constant conditions is presented in Fig. 8. Here, the temperature is stabilized at $35°C$ and the intensity is set at 950 $(W/Sq.m)$ whereas the solar voltage is stabilized at 190.7 V and the current is maintained at 66.22 A throughout the system.

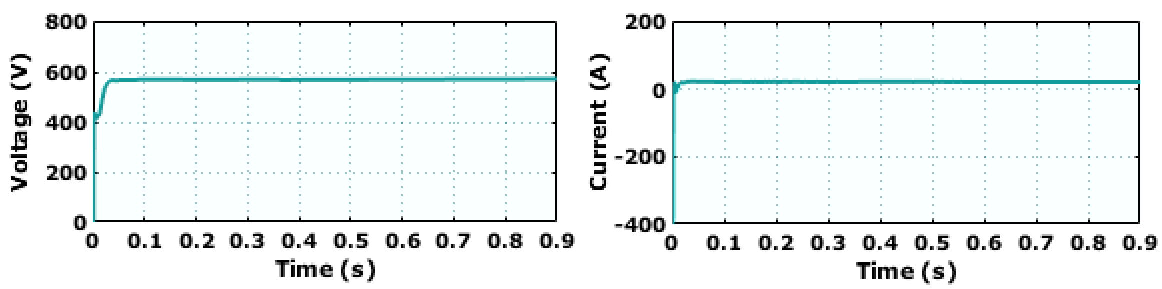

Fig. 9. Outputs of CISC converter

The CISC converter's outputs are displayed in Fig. 9, where the output side voltage is settled at 571.8 V and the output side current is kept constant at 21.5 A all over the system.

10.22060/EEJ.2026.25681.5987

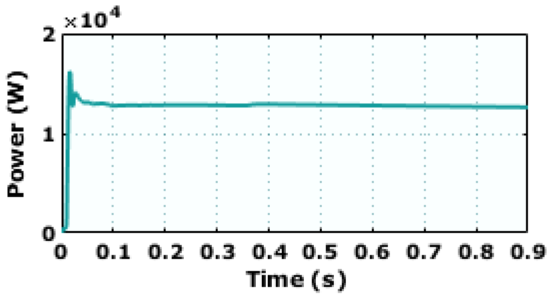

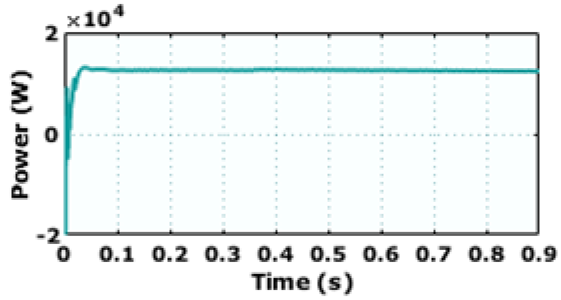

Fig. 10. Waveform of power

The power waveform is depicted in Figure 10, where the system's output power is maintained at 14000 W while the input power is stabilized at 15000 W.

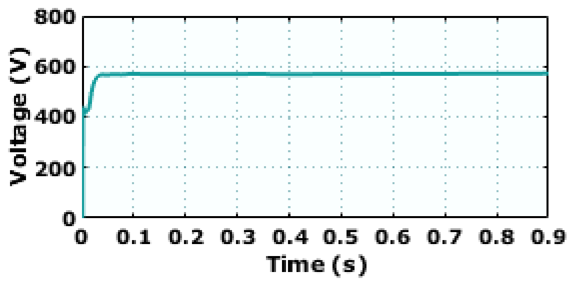

Fig. 11. Waveform of DC link

As depicted in Fig. 11, the voltage on the DC link is stabilized at 550 V. The battery and BLDC motor also receive this voltage.

10.22060/EEJ.2026.25681.5987

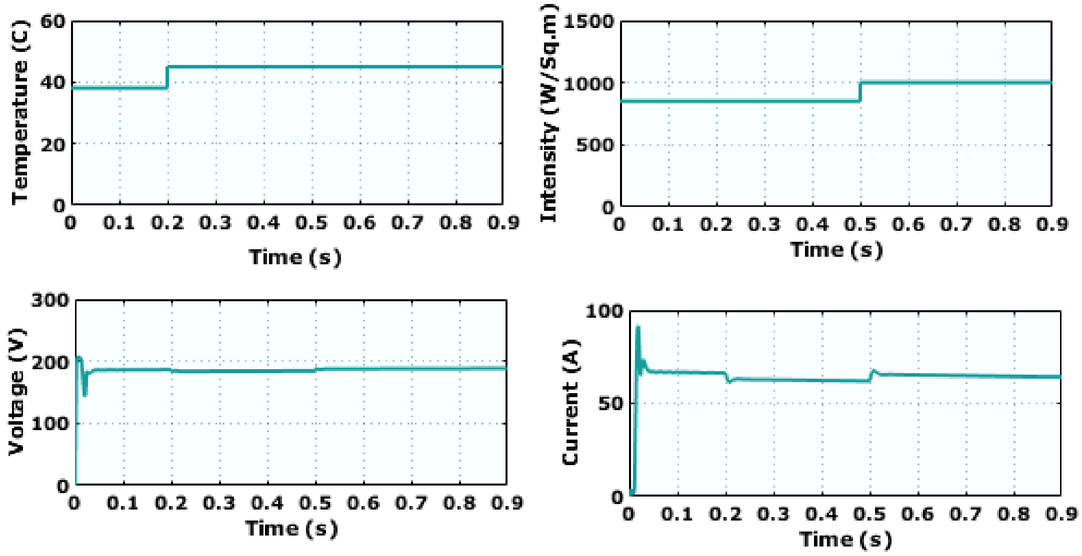

Fig. 12. Waveform of PV system in varying condition

The solar module response waveform in a varying setting is shown in Fig. 12, where the intensity is kept at $1000\,(W/Sq.m)$ all over the entire system and the temperature is settled at $45°C$ following the initial fluctuations. After then, the system's total current settles at 70 A while the voltage is maintained at 190 V.

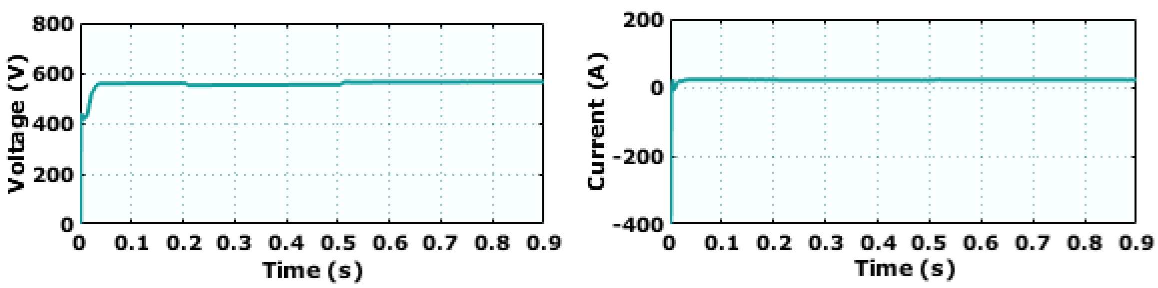

Fig. 13. Outputs of CISC converter

The outputs of a CISC converter are presented in Fig. 13. The output side voltage is settled at 15000 W, and the current is 14000 W.

10.22060/EEJ.2026.25681.5987

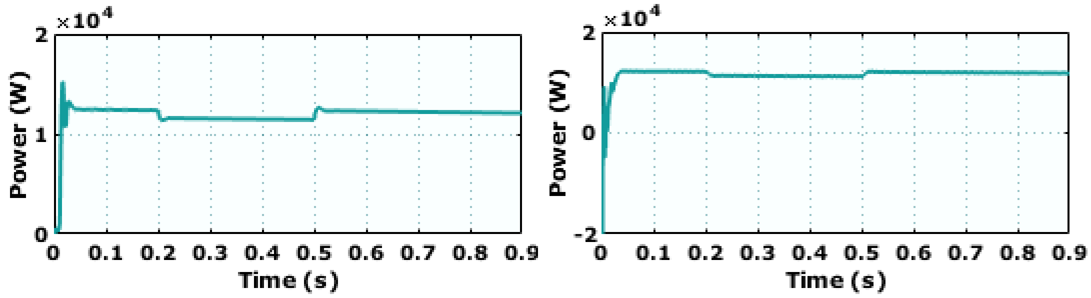

Fig. 14. Waveform of power

Fig. 14 reveals the power behaviour. The system's output power is stabilized at 14000 W while the input power is sustained at 15000 W.

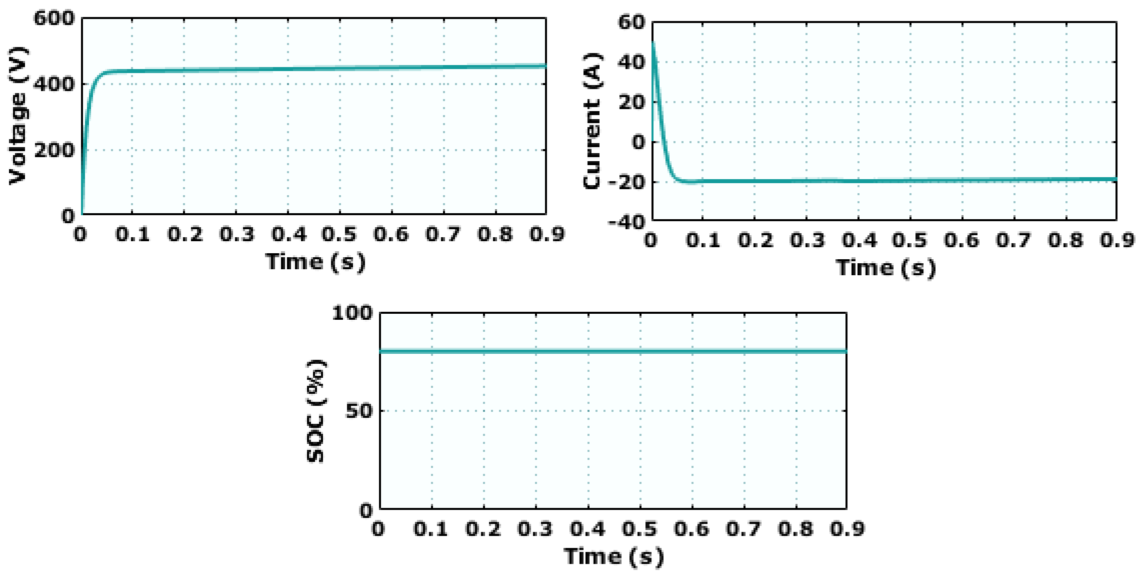

Fig. 15. Waveform of battery

While the current is maintained at -20 A, the battery voltage is progressively increased and stabilised at 430 V. As displayed in Fig. 15, the SOC is then stabilized at 80%.

10.22060/EEJ.2026.25681.5987

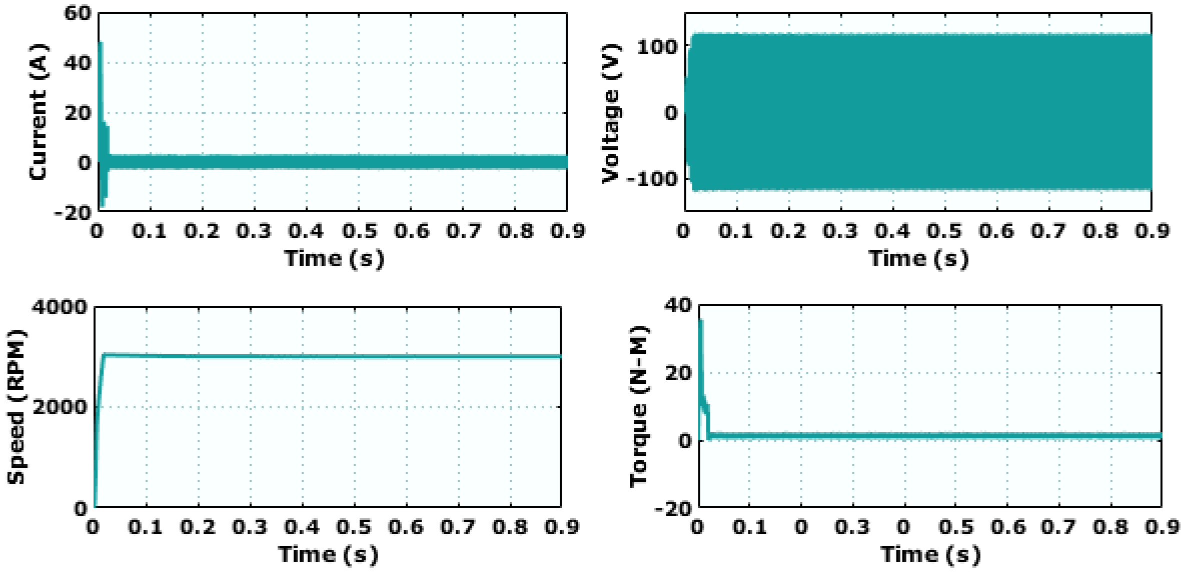

Fig. 16. Waveform of BLDC motor

The BLDC motor responses are depicted in Fig. 16. This results in greater efficacy since the motor current is 3A and the back EMF is 80 V whereas the voltage is settled at 80 V and the motor speed is sustained at 3000 RPM.

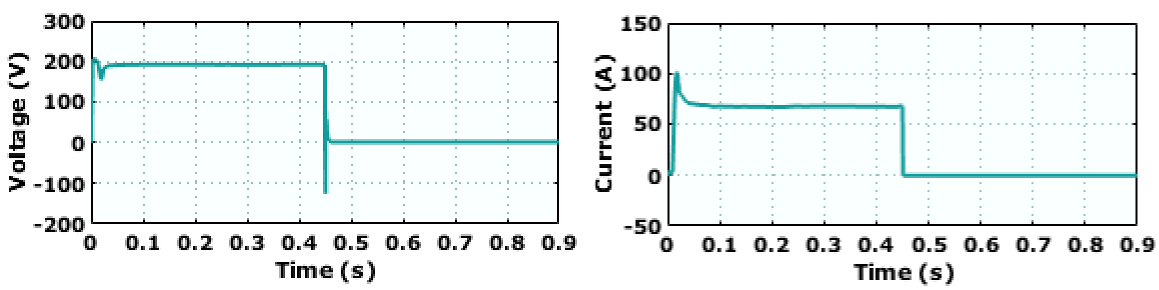

Fig. 17. Waveform of PV system when PV system is shutdown

As depicted in Fig. 17, the battery powers the BLDC motor whereas the PV power is switched off at 0.45 seconds. Both the solar current and the PV voltage are lowered and stabilised at lesser values.

10.22060/EEJ.2026.25681.5987

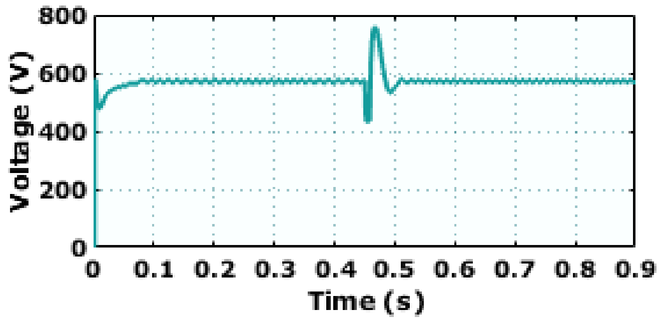

Fig. 18. Waveform of DC link

Fig. 18 presents the DC link voltage behaviour. There are minimal variations in the DC link voltage, which is sustained at 580 V.

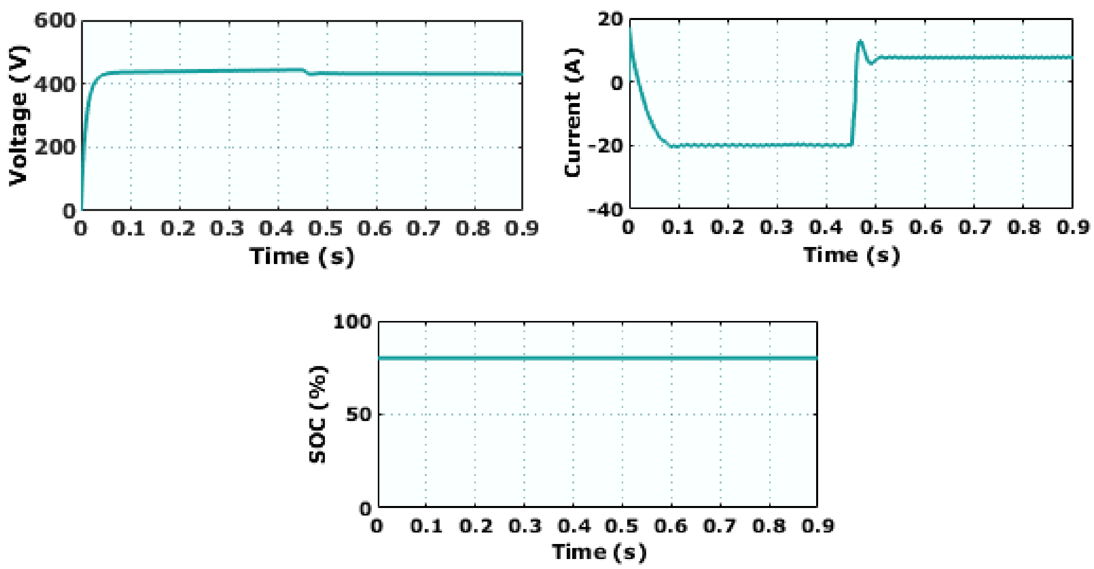

Fig. 19. Waveform of battery

While the current is maintained at -20 A, the battery voltage is progressively increased and settled at 430 V. As displayed in Fig. 19, the SOC is then stabilized at 80%.

10.22060/EEJ.2026.25681.5987

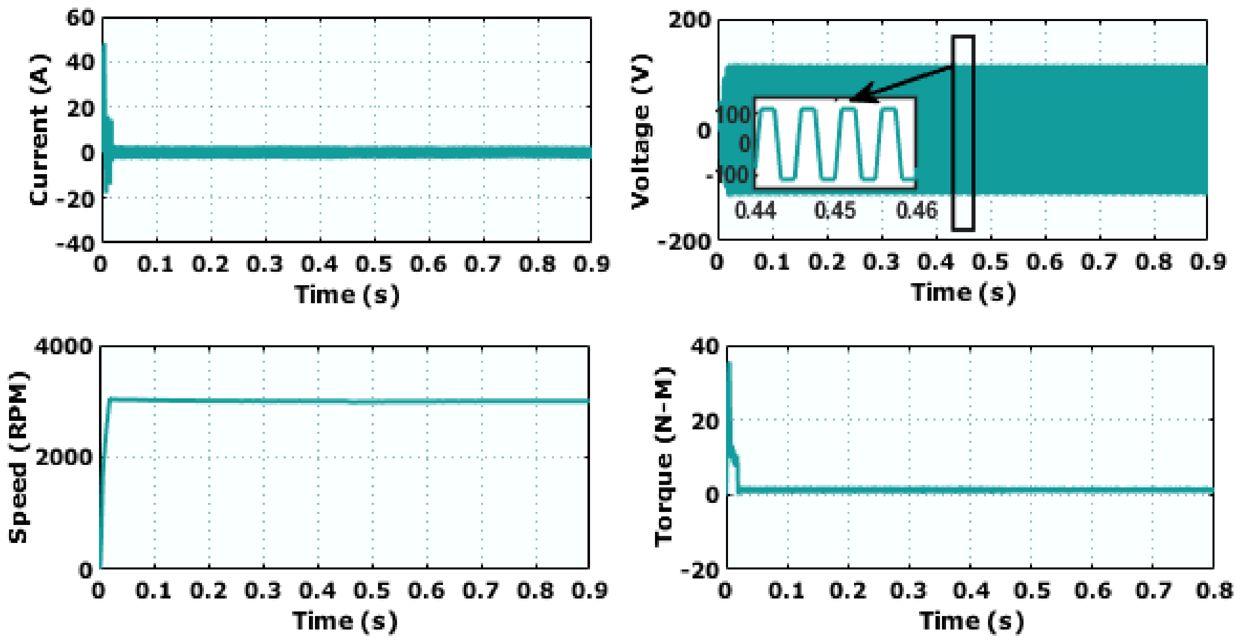

Fig. 20. Waveform of BLDC motor

Fig. 20 represents the BLDC motor's responses. Here, the battery EMF is settled at 80 V while the motor current is sustained at 2 A. As a result, the torque is set at 2A across the system and the motor speed is maintained at 3000 RPM. An analysis of numerous cases are represented in Table 4.

Table 4 Analysis of numerous cases

SCENARIO	TEMPERATURE	INTENSITY	PV VOLTAGE	PV CURRENT
CONSTANT	35℃	950 $(W/Sq.m)$	190.7 V	66.22 A
VARYING	45℃	1000 $(W/Sq.m)$	190 V	70 A
PV SYSTEM SHUT DOWN	-	-	3 V	3A

10.22060/EEJ.2026.25681.5987

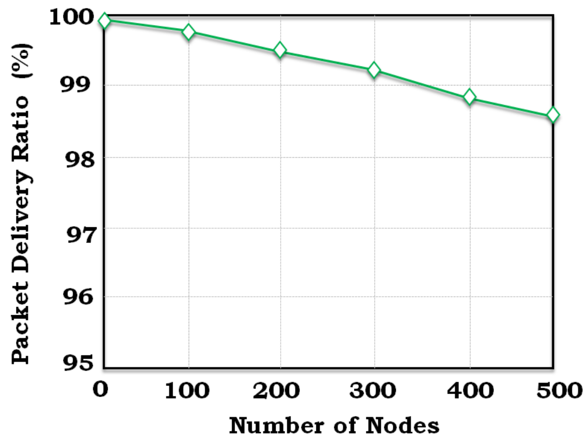

Fig. 21. PDR

The Packet Delivery Ratio (PDR) of the routing algorithms is shown in Figure 21. With an average of 99.15%, the SFOA–ANN routing regularly attains the highest PDR, ranging from 99.58% at 100 nodes to 98.69% at 500 nodes. By avoiding energy-depleted nodes, SFOA's intelligent route selection in conjunction with ANN-based decision making diminishes packet losses.

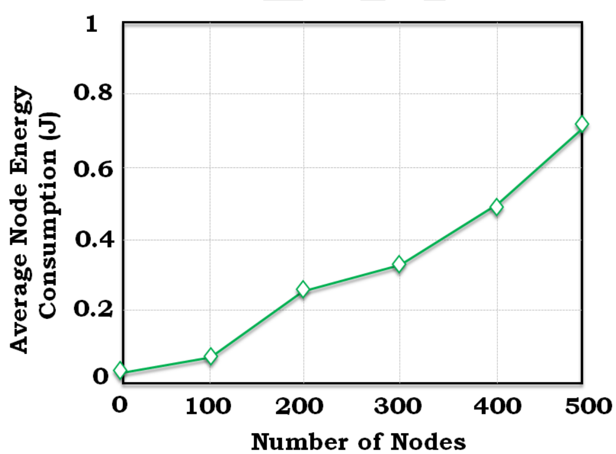

Fig. 22. Energy consumption

The average node energy consumption is depicted in Figure 22. The SFOA–ANN method uses 0.12 J at 100 nodes and 0.69 J at 500 nodes. The ANN dynamically chooses energy-efficient routing paths based on network conditions, while SFOA's optimisation ability effectively lowers needless transmissions. As a

10.22060/EEJ.2026.25681.5987

consequence, for IoT-enabled solar-powered EV monitoring systems, the SFOA–ANN approach increases network lifetime and boosts energy efficiency.

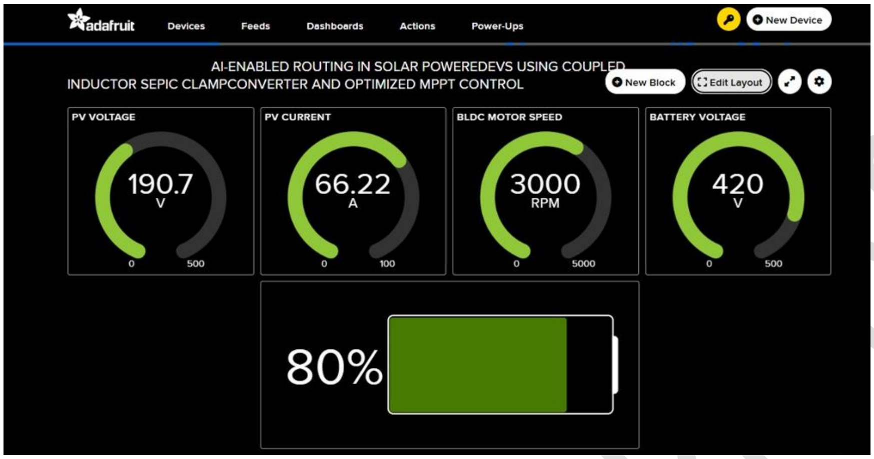

Fig. 23. IoT result

The IoT display of the suggested research's monitored performance is depicted in Fig. 23. While the PV current and voltage are 66.22 A and 190.7 V, the motor speed and battery voltage are 3000 RPM and 420 V.

Table 5. Comparison of efficiency

CONVERTERS	VOLATGE GAIN	EFFICIENCY in%
Non-Isolated High Step-Up [14]	$\frac{1}{1+D+n}$	94.35
High Step-Up Boost-Cuk [15]	$\frac{1+D}{D(3+D)}$	90.7
High-Gain Buck-Boost-Cuk [16]	$\frac{1}{(1+n)(1+D)}$	93.8
Transformer less Active Switched Inductor and Capacitor Cuk [17]	$\frac{1}{5-D}$	97.03
High Step-Up Interleaved Boost-Cuk [18]	$\frac{1}{3+D+n_1+n_2}$	94.01
Proposed	$\frac{1+n}{1-D}$	97.3

Table 5 reveals that the Non-Isolated High Step-Up Converter has an efficiency of 94.35%, representing dependable operation but with discernible power losses. Out of all the converters, the High Step-Up Boost-Cuk Converter has the lowermost efficiency at 90.7%. Greater switching and conduction losses are the cause of this. The High-Gain Buck Boost–Cuk Converter provides enhanced performance with further loss

10.22060/EEJ.2026.25681.5987

reduction at an efficiency of 93.8%. By reducing switching and conduction losses, the proposed converter outperforms all existing converters with the highest efficacy of 97.3%.

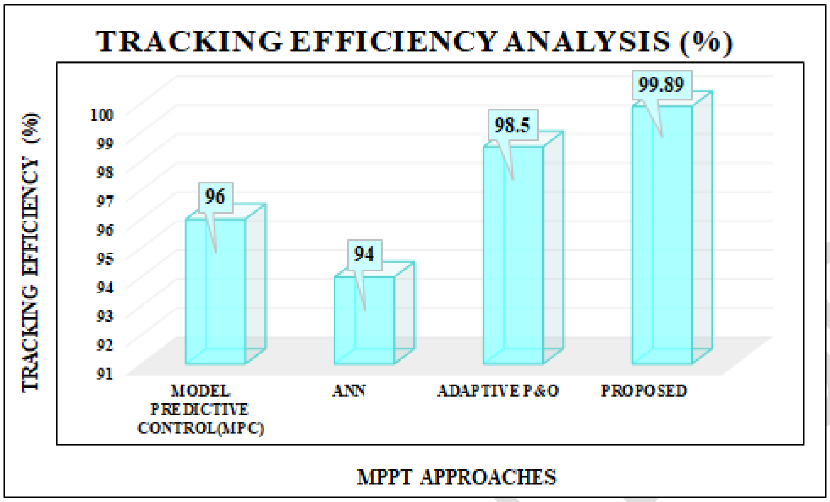

Fig. 24. Comparison of tracking efficiency

As represented in Fig. 24, the developed approach have superior performance than other approaches with a tracking efficiency of 99.89%. The Adaptive P&O [20] method performed well, with an efficiency of 98.5%. The MPC [21] methodology attains an efficiency of 96% when compared to the more complex methods. The ANN [25] approach has the lowest tracking efficiency (94%), representing its relatively low efficacy in preserving steady tracking precision. By decreasing steady-state error and dynamic deviations, the proposed method enhances system stability and overall performance in real-time applications.

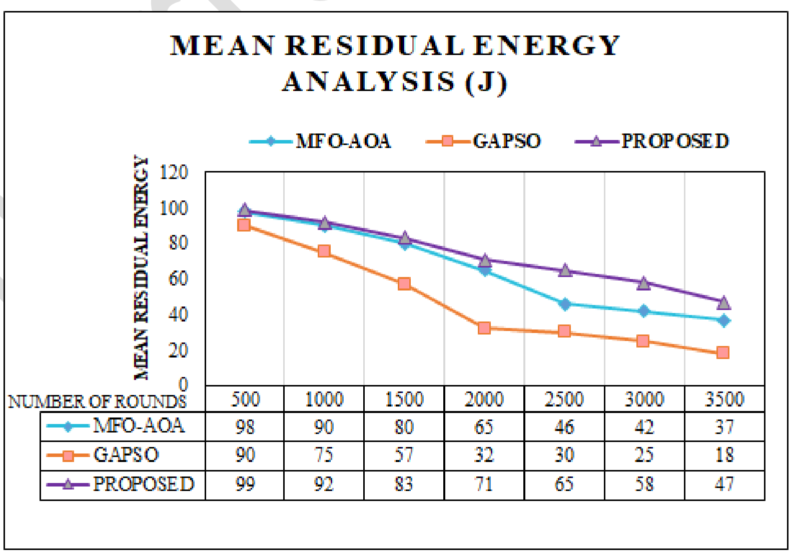

NUMBER OF ROUNDS	500	1000	1500	2000	2500	3000	3500
MFO-AOA	98	90	80	65	46	42	37
GAPSO	90	75	57	32	30	25	18
PROPOSED	99	92	83	71	65	58	47

Fig. 25. Analysis of mean residual energy

10.22060/EEJ.2026.25681.5987

Figure 25 displays the mean residual energy analysis of numerous routing algorithms. The SFOA-ANN routing strategy reliably preserves a higher mean residual energy than MFO-AOA [38] and GA-PSO [39]. The SFOA's enhanced routing paths aid in lowering unnecessary transmissions, whereas the ANN adjusts routing decisions in response to network circumstances. Conversely, GA-PSO shows the fastest rate of energy depletion, signifying less effective energy management. It confirms that in IoT-based EV monitoring systems, the SFOA-ANN approach significantly increases network longevity and energy efficiency.

Table 6. Comparison of packet delay

NUMBER OF NODES	MFO-AOA [38]	GAPSO [39]	PROPOSED
100	30	42	20
200	45	55	23
300	60	78	41
400	82	90	73
500	98	110	87

Table 6 compares the packet delay of MFO-AOA, GAPSO and the proposed approach. The proposed method has the lowest value of 20 at 100 nodes, outperforming MFO-AOA and GAPSO. As the network expands to 200 and 300 nodes, the proposed approach keeps showing lower values, representing higher efficiency. Even at higher densities of 400 and 500 nodes, the suggested method preserves lower performance metrics.

Table 7. Statistical Performance

Metrics	Mean	Median	SD
PDR in %	99.15	99.17	0.18
Packet Delay in ms	20.0	20.1	0.63
Mean Residual Energy (J)	1.63	1.64	0.04
Network Lifetime (Rounds)	2068	2067	18.7

The MATLAB simulations are run 30 times independently with various random initial populations under the same operating conditions to assess the resilience of the SFO–RBFIS–MPPT and SFOA–ANN routing algorithms. The statistical outcomes show very minute standard deviations for all performance indicators, signifying that the suggested optimisation methodology has good repeatability and robust convergence, as depicted in Table 7. Additionally, the substantial residual energy and consistently low packet latency

10.22060/EEJ.2026.25681.5987

demonstrate the computational stability and dependability of the AI-enabled energy management and routing technique.

Table 8. Comparison of time complexity analysis

APPROACHES	SD	MEDIAN	MEAN
MFO-AOA [38]	0.1610	1.9084	1.8947
GA-PSO [39]	0.2042	2.2115	2.2340
PROPOSED	0.1343	1.7640	1.3467

The SFOA-ANN has the lowest standard deviation than MFO-AOA and GA-PSO, representing more dependable and consistent performance, as presented in Table 8. Furthermore, the developed approach has the lowest central tendency median value, signifying greater overall efficacy. The significantly reduced mean value further demonstrates the effectiveness of the developed approach in reducing performance costs. Conversely, GA-PSO exhibits the highest mean, median and SD, portentous a lesser optimisation efficiency. For IoT-EV monitoring systems, it aids the reliability and robustness of the SFOA-ANN routing approach.

5. Conclusion

This research proposes a CISC converter, an optimised RBFIS-MPPT controller and AI- routing to an intelligent energy management framework. By efficiently optimising the RBFIS settings, the SFO algorithm track the global maximum power point precisely and quickly in a range of temperature and irradiance conditions. The CISC converter ensures a reliable DC-link for the motor drive and battery interface by attaining high voltage gain while reducing input current ripple, switch voltage stress and conversion losses. To optimise energy use and rise the vehicle's driving range, an SFOA-ANN routing algorithm intelligently manages power flow between the PV array, battery and BLDC motor. Results using MATLAB reveal earlier convergence, less steady-state oscillations, efficient battery energy management and a 97.3% converter efficiency. The developed framework is a viable solution for intelligent and sustainable electric vehicles of the future since it greatly increases the efficiency and scalability of solar-powered EV systems.

References

[1] S. Gomathi, Power Management Comparison in DC -DC Converters for Electric Vehicles, 2024 8th International Conference on Electronics, Communication and Aerospace Technology (ICECA), Coimbatore, India, (2024) 178-182.

[2] N. H. Alrasheedi, A. Karthick, P. M. Kumar, V. Rajendran, Performance Study of Nano-Enhanced PCM in Building-Integrated Semi-Transparent Photovoltaic Modules, Buildings, 15(23) (2025) 4236.

[3] K. S. Kavin, P. Subha Karuvelam, M. Devesh Raj, M. Sivasubramanian, A novel KSK converter with machine learning MPPT for PV applications, Electric power components and systems, (2024) 1-19.

[4] M. A. Prabhu, G. E. Sheela, H. Alzahrani, H. Siddiq, A. Okmi, N. Alharbi, S. S. Florence, M. S. Lekshmy, S. Velayuthan Pillai, Green synthesis of ZnO, Fe3O4, and TiO2 nanoparticles: exploring enhanced bacterial inhibition, catalysis, and photocatalysis for sustainable environmental applications, International Journal of Environmental Analytical Chemistry, (2025) 1-25.

[5] B. Mohan, M. V. Ramesh, M. Seshu, P. M. Kumar, M. Valavala, Design And Implementation Of Electric Vehicle Charging Station Integrated With Different Energy Sources Using Anfis Controller, Journal of Theoretical and Applied Information Technology, 103(4) (2025) 1245-1255.

[6] S. Sharma, K. M. Krishna, S. S. Joshi, M. Radhakrishnan, S. Palaniappan, S. Dussa, R. Banerjee, N. B. Dahotre, Laser based additive manufacturing of tungsten: Multi-scale thermo-kinetic and thermo-mechanical computational model and experiments, Acta Materialia, 259 (2023) 119244.

[7] A. R. Singh, R. S. Rathore, W. Jiang, A. Thakare, R. S. Kumar, C. B. Khadse, H. K. Addis, A scalable cloud-integrated AI platform for real-time optimization of EV charging and resilient microgrid energy management, Scientific Reports, 15(1) (2025) 37692.

[8] S. Hussain, A. Sami, A. Thasin, R. M. Saad, AI-Enabled Ant-Routing Protocol to Secure Communication in Flying Networks, Applied Computational Intelligence and Soft Computing, 2022(1) (2022) 3330168.

[9] S. Esmaeili, M. Shekari, M. Rasouli, S. Hasanpour, A. A. Khan, H. Hafezi, High gain magnetically coupled single switch quadratic modified SEPIC DC-DC converter, IEEE Transactions on Industry Applications, 59(3) (2023) 3593-3604.

[10] M. Harasimczuk, R. Kopacz, A. Tomaszuk, Lossless clamp circuit with turn-off voltage and current reduction in high step-up dc–dc converter with coupled inductor, IEEE Transactions on Power Electronics, 39(1) (2023) 1074-1086.

[11] M. D. O. Vasconcelos Junior, F. Carneiro de Araujo, A. A. Alencar Freitas, M. V. S. Costa, F. L. Tofoli, F. L. Marcelo Antunes, E. Mineiro Sá Jr, K. C. Alves de Souza, Nonisolated High Step-Up DC-DC Ćuk Converter Based on Coupled Inductors, International Journal of Circuit Theory and Applications, (2025).

[12] M. V. M. Ewerling, T. B. Lazzarin, C. H. Illa Font, Modular SEPIC-Based Isolated dc–dc Converter with Reduced Voltage Stresses across the Semiconductors, Energies, 15(21) (2022) 7844.

[13] K. Karimi, E. Babaei, M. Karimi, D. Alizadeh, S. M. J. Mousavi, An interleaved high step-up DC–DC converter based on coupled-inductor, IET Power Electronics, 17(3) (2024) 473-485.

[14] A. A. Alencar Freitas, F. Carneiro de Araújo, F. A. Pereira Aragão, K. C. Alves de Souza, F. L. Tofoli, E. Mineiro Sá Jr, F. Luiz Marcelo Antunes, Non- Isolated High Step- Up DC–DC Converter Based on Coupled Inductors, Diode- Capacitor Networks, and Voltage Multiplier Cells, In ternational Journal of Circuit Theory and Applications, 50(3) (2022) 944–963.

[15] H. Li, L. Cheng, X. Sun, C. Li, High Step- Up Combined Boost- Cuk Converter with Switched-Inductor, IET Power Electronics, 15(15) (2022) 1664–1674.

[16] D. Rong, N. Wang, X. Sun, H. Dong, High- Gain Combined Buck- Boost- Cuk Converter With Coupled Inductance, IET Power Elec tronics, 15(2) (2022) 132–144.

[17] A. M. S. S. Andrade, T. M. K. Faistel, A. Toebe, R. A. Guisso, Family of Transformerless Active Switched Inductor and Switched Capacitor Ćuk DC–DC Converter for High Voltage Gain Applications, IEEE Journal of Emerging and Selected Topics in Industrial Electronics, 2(4) (2021) 390–398.

[18] D. Rong, X. Sun, N. Wang, A High Step- Up Interleaved Boost- Cuk Converter With Integrated Magnetic Coupled Inductors, IET Re newable Power Generation, 16(3) (2022) 607–621.

[19] V. Kumar, R. K. Bindal, MPPT technique used with perturb and observe to enhance the efficiency of a photovoltaic system, Materials Today: Proceedings, 69 (2022) A6-A11.

[20] B. Naima, B. Belkacem, T. Ahmed, H. Benbouhenni, B. Riyadh, H. Samira, Z. Sarra, Z. M. S. Elbarbary, S. A. Mohammed, Enhancing MPPT optimization with hybrid predictive control and adaptive P&O for better efficiency and power quality in PV systems, Scientific reports, 15(1) (2025) 24559.

[21] Y. Zhao, A. An, Y. Xu, Q. Wang, M. Wang, Model predictive control of grid-connected PV power generation system considering optimal MPPT control of PV modules. Prot. Control Mod, Power Syst, 6 (2021)1-12.

[22] D. A. Asoh, B. D. Noumsi, E. N. Mbinkar, Maximum power point tracking using the incremental conductance algorithm for PV systems operating in rapidly changing environmental conditions, Smart Grid and Renewable Energy, 13(5) (2022) 89-108.

10.22060/EEJ.2026.25681.5987

[23] N. Priyadarshi, M. S. Bhaskar, P. Sanjeevikumar, F. Azam, B. Khan, High-power DC-DC converter with proposed HSFNA MPPT for photovoltaic based ultra-fast charging system of electric vehicles, IET Renewable Power Generation, 19(1) (2025) e12513.

[24] S. Manna, D. K. Singh, A. K. Akella, H. Kotb, K. M. AboRas, H. M. Zawbaa, S. Kamel, Design and implementation of a new adaptive MPPT controller for solar PV systems, Energy Reports, 9 (2023) 1818-1829.

[25] H. Bozkurt, Ö. Çelik, A. Teke, Power quality enhancement in hybrid PV-BES system based on ANN-MPPT, Turkish J. Electr. Eng. Comput. Sci., 32(5) (2024) 662–681.

[26] A. S. Kumar, S. Ramesh, P. Arukula, M. A. S. Parveen, Analyzing PV power systems using MPPT based on Artificial Neural Networks, Nanotechnol. Percept, 20 (2024) 792-797.

[27] M. H. Osman, M. A. E. Seify, M. K. Ahmed, N. V. Korovkin, A. Refaat, Highly efficient MPP tracker based on adaptive neuro-fuzzy inference system for stand-alone photovoltaic generator system, Int. J. Renew. Energy Res, 12(1) (2022) 209-217.

[28] E. Artetxe, J. Uralde, O. Barambones, I. Calvo, I. Martin, Maximum power point tracker controller for solar photovoltaic based on reinforcement learning agent with a digital twin, Mathematics, 11(9) (2023) 2166.

[29] H. Alhusseini, L. M. Abdali, H. A. Issa, V. I. Velkin, Adaptive particle swarm optimization based model predictive control MPPT algorithm for PV systems under partial shading conditions, Results in Engineering, (2025) 107419.

[30] R. Celikel, M. Yilmaz, A. Gundogdu, Improved voltage scanning algorithm based MPPT algorithm for PV systems under partial shading conduction, Heliyon, 10(20) (2024).

10.22060/EEJ.2026.25681.5987

[31] M. A. E. Mohamed, S. Nasser Ahmed, M. Eladly Metwally, Arithmetic optimization algorithm based maximum power point tracking for grid-connected photovoltaic system, Scientific Reports, 13(1) (2023) 5961.

[32] M. J. Abbass, R. Lis, F. Saleem, The maximum power point tracking (MPPT) of a partially shaded PV array for optimization using the antlion algorithm, Energies, 16(5) (2023) 2380.

[33] N. K. Musham, R. Hemnath, Real-time path planning for IoT-enabled autonomous vehicle robotics using RRT and A* algorithms, International Journal of Multidisciplinary Research and Explorer, 5(1) (2025) 66-84.

[34] S. Boubaker, S. Al-Dahidi, S. Kamel, N. Ghazouani, H. Kraiem, F. S. Alsubaei, F. Bourennani, W. Meskine, M. Benghanem, A. Mellit, Electric vehicles charging station allocation based on load profile forecasting and Dijkstra's algorithm for optimal path planning, Scientific Reports, 15(1) (2025) 23844.

[35] X. Xue, R. Shanmugam, S. Palanisamy, O. I. Khalaf, D. Selvaraj, G. M. Abdulsahib, A hybrid cross layer with harris-hawk-optimization-based efficient routing for wireless sensor networks, Symmetry, 15(2) (2023) 438.

[36] Z. Wang, Z. Jin, Z. Yang, W. Zhao, M. Trik, Increasing efficiency for routing in internet of things using binary gray wolf optimization and fuzzy logic, Journal of King Saud University-Computer and Information Sciences, 35(9) (2023) 101732.

[37] Mohseni, M., Amirghafouri, F. and Pourghebleh, B., "CEDAR: A cluster-based energy-aware data aggregation routing protocol in the internet of things using capuchin search algorithm and fuzzy logic." *Peer-to-peer networking and applications* 16, no. 1 (2023): 189-209.

10.22060/EEJ.2026.25681.5987

[38] G. Natesan, S. Konda, R. P. de Prado, M. Wozniak, A hybrid mayfly-aquila optimization algorithm based energy-efficient clustering routing protocol for wireless sensor networks, Sensors, 22(17) (2022) 6405.

[39] B. M. Sahoo, H. M. Pandey, T. Amgoth, GAPSO-H: A hybrid approach towards optimising the cluster based routing in wireless sensor network, Swarm Evol. Comput, 60 (2021) 100772.